

## Mechanics of crystalline boron nanowires

Weiqliang Ding<sup>a</sup>, Lorenzo Calabri<sup>b</sup>, Xinqi Chen<sup>a</sup>, Kevin M. Kohlhaas<sup>a</sup>, Rodney S. Ruoff<sup>a,\*</sup>

<sup>a</sup> Department of Mechanical Engineering, Northwestern University, Evanston, IL 60208, United States

<sup>b</sup> Dipartimento di meccanica e tecnologie industriali, Universita di Firenze, Via di Santa Marta 50139, Florence, Italy

Received 21 August 2005; received in revised form 28 October 2005; accepted 16 November 2005

Available online 19 January 2006

### Abstract

The mechanical response of crystalline boron nanowires was studied with the mechanical resonance method and tensile testing. The mechanical resonances of cantilevered boron nanowires were excited and their frequencies were used to obtain the Young's modulus of the nanowires, according to simple beam theory. The influence of non-ideal boundary conditions on the nanowire's resonance frequency was investigated and is presented. Tensile loading measurements on boron nanowires were performed to obtain the fracture strength and Young's modulus. The modulus values from tensile tests are consistent with the set of values obtained from the mechanical resonance tests. © 2005 Elsevier Ltd. All rights reserved.

**Keywords:** A. Nanostructures; B. Fracture; B. Mechanical properties; B. Strength; B. Vibration

### 1. Introduction

One-dimensional nanostructures such as nanotubes and nanowires have attracted attention in the past due to the promise of applications in sensing [1,2], materials reinforcement [3–6], and nanoelectronics [7–11]. They can serve as electrical interconnects [7,9,10], and building blocks in microelectromechanical or nanoelectromechanical systems (MEMS and NEMS) [12–14].

Boron (B) is a unique element, which in elemental boron solids exhibits structural complexity due to its electron-deficient bond [15]. The boron solids have high melting points, low density, high modulus, and high hardness [16,17]. Crystalline B nanowires have been synthesized by the chemical vapor deposition (CVD) method onto preformed metal catalyst particles [18]. Study of their electrical transport showed *p*-type semiconductor behavior [7] and rectification [9]. To further develop both a fundamental understanding and applications for these crystalline nanowires, it is important to study their mechanical properties. In this work, the mechanical resonance method and tensile loading were used to characterize the stiffness and strength of B nanowires.

The mechanical resonance method is a non-destructive method for determining the bending modulus of beam-shaped structures. It has been used to study the mechanical properties of nanotubes [19,20], nanowires [21] and nanobelts [22]. Mechanical resonance can be induced in a nanowire when the frequency of the applied periodic force approaches the nanowire's resonance frequency. According to simple beam theory [23], the *n*th mode frequency,  $f_n$ , of a cantilevered uniform beam is

$$f_n = \frac{\beta_n^2}{2\pi} \sqrt{\frac{E_b I}{m L^4}}, \quad (1)$$

where  $E_b$  is the bending modulus of the beam,  $I$  is the cross-section moment of inertia,  $m$  is the unit mass, and  $L$  is the beam length. The  $\beta_n$  term is the eigenvalue from the characteristic equation:  $\cos \beta_n \cosh \beta_n + 1 = 0$ ;  $\beta_0 = 1.875$ ,  $\beta_1 = 4.694$ ,  $\beta_2 = 7.855$  and  $\beta_3 = 10.996$  correspond to the first four resonance modes for any cantilevered beam. For a solid beam with circular cross-section, the mechanical resonance frequency is

$$f_n = \frac{\beta_n^2}{2\pi} \frac{D}{L^2} \sqrt{\frac{E_b}{16\rho}}, \quad (2)$$

where  $\rho$  is the beam density and  $D$  is the beam diameter.

\* Corresponding author. Tel.: +1 847 467 6596; fax: +1 847 491 3915.  
E-mail address: [r-ruoff@northwestern.edu](mailto:r-ruoff@northwestern.edu) (R.S. Ruoff).

Uniaxial tensile loading has been previously used to measure the fracture strength of nanotubes [24] and nanofibers [25–27]. During quasi-static tensile loading, a continuously increasing tensile load is typically applied to a specimen until it fractures. The specimen's elongation and the applied load are recorded during the tensile loading process. With knowledge of the specimen geometry, the Young's modulus, tensile strength, and other tensile properties such as fracture strength and failure strain of the material can be determined.

## 2. Boron nanowire source

The CVD-synthesized B nanowires were typically tens of micrometers in length [18]. Their diameters varied from 20 to 200 nm with a mean value of 60 nm [18]. Fig. 1(a) shows a SEM image of as-grown boron nanowires on an alumina substrate.

Since the mechanical measurements presented in this paper are to be performed on individual nanowires, the nanowires need to be well separated. However, as shown in Fig. 1(a), the CVD-synthesis process produced clusters of B nanowires, making it difficult to directly manipulate

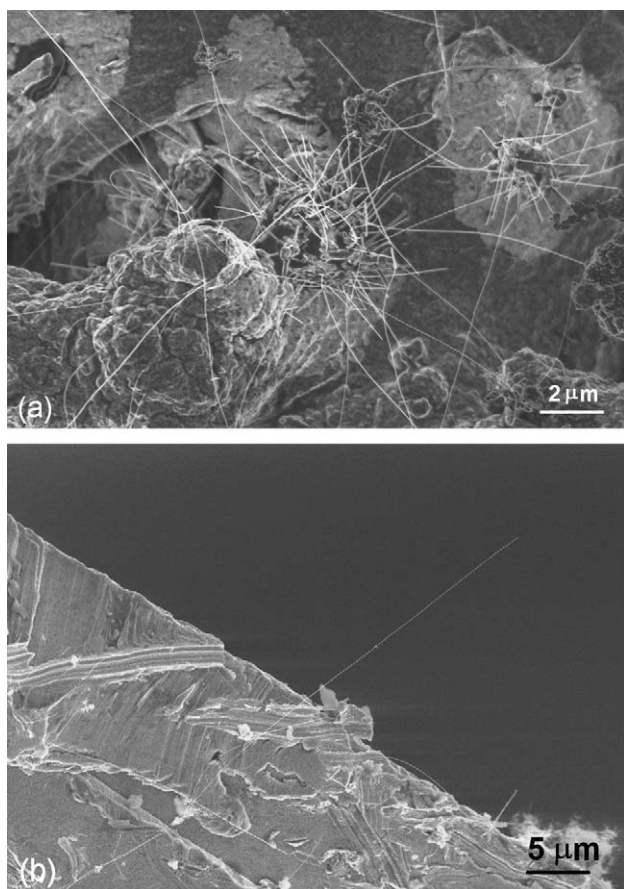


Fig. 1. (a) SEM image of CVD grown crystalline B nanowires on alumina substrate; (b) A B nanowire protruding outward at the ledge of a cut copper TEM grid.

individual ones. A mesh copper TEM grid (PELCO®Grids, 200 square mesh, Ted Pella, Inc. Redding, CA) was used to pick up individual nanowires from the source. The grid was first cut in half with a razor blade, and the cut edge was brushed along the alumina surface where the B nanowires were grown. Some B nanowires adhered to the TEM grid with many of them protruding from the cut edge (Fig. 1(b)), which enabled straightforward pickup with AFM cantilever tips for mechanical testing using our home-built nanomanipulator [28]. The electron beam induced deposition (EBID) method was used to clamp the B nanowire to the AFM tip inside a SEM vacuum chamber prior to mechanical testing [29].

## 3. Mechanical resonance test

### 3.1. Resonance test experimental setup

Mechanical resonance tests were performed inside a LEO 1525 field emission gun SEM with our home-built nanomanipulator. A conductive ultra-sharp AFM cantilever (NSC 12 with 30 nm Ti/Pt coating, MikroMasch Inc.) and the nanowire source (the cut TEM grid) were attached to the two opposing positioning stages of the nanomanipulator. The AFM cantilever was mounted on the end of a piezoelectric multi-layer bender (Noliac A/S, Denmark, ceramic multilayer bender B1) that was mounted to the X–Y linear motion stage; the B nanowire source (TEM grid) was fixed to the Z linear motion stage. The cantilever and copper TEM grid were both electrically insulated from the nanomanipulator.

During resonance measurements, a cantilevered B nanowire was excited into mechanical resonance by applying a periodic force that was either electrically or mechanically induced. For electrical excitation (Fig. 2(a)), a function generator (Stanford Research Systems, California, Model DS345) applied an ac voltage with tunable frequency between the AFM cantilever and the copper TEM grid. For mechanical excitation (Fig. 2(b)), an ac voltage was applied to the piezoelectric bender to induce mechanical vibration, which drove mechanical resonance in the attached nanowire. For mechanically induced resonance, the frequency of the applied ac signal is the nanowire's natural frequency. The situation for electrically induced resonance is discussed below.

Most of the B nanowires we tested were first clamped to the tip of the AFM cantilever using EBID, and then removed from the source. Nanowires protruding from the edge of the TEM grid can also be electrically excited into resonance (Fig. 2(a)).

### 3.2. Resonance test data analysis

During resonance measurements, the driving frequency from the function generator was swept and the nanowire's frequency response was recorded. The first resonance mode of the cantilevered nanowires was easily excited; the second

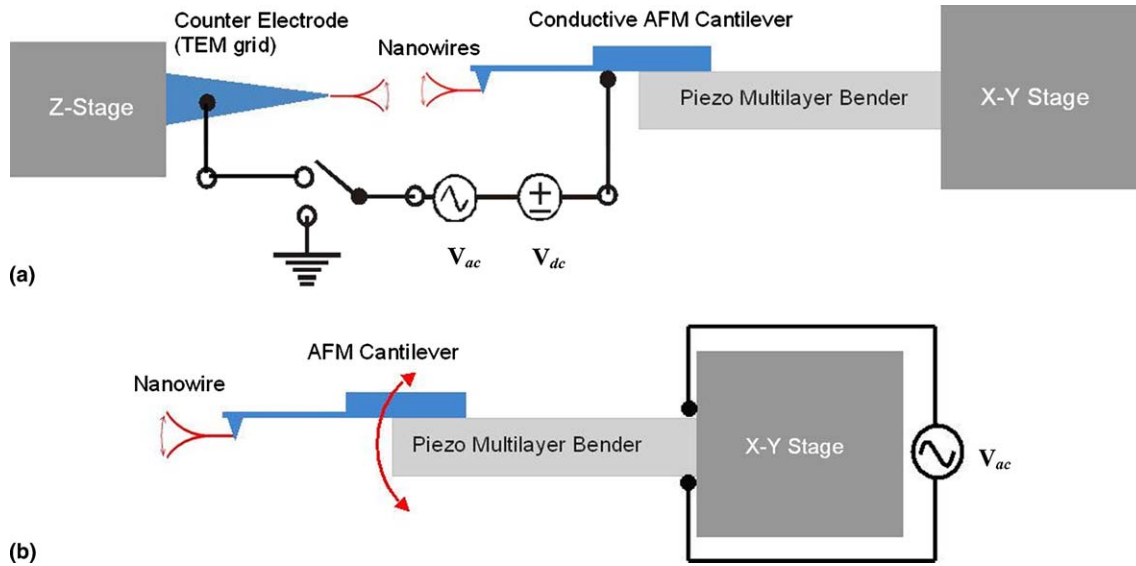


Fig. 2. (a) Electrical excitation of cantilevered nanowires attached either to a conductive AFM cantilever tip or to a copper TEM grid. (b) Mechanical excitation of a cantilevered nanowire attached to an AFM cantilever tip.

and higher order modes were only observed for nanowires with aspect ratios (length divided by width) typically greater than 200. This is discussed further below. Fig. 3(a) shows SEM images of the first two harmonic resonance modes of a cantilevered B nanowire attached to an AFM tip.

The frequency responses of resonating nanowires were recorded during the experiments. Later the resonance peaks were obtained through data fitting. Fig. 3(b) shows a typical frequency response curve of the first resonance mode. The quality factors ranged from  $300$  to  $1000$  inside the SEM vacuum chamber (pressure  $10^{-6}$  to  $10^{-7}$  Torr). The second and higher resonance modes of several B nanowires were also observed. As shown in Fig. 3(c), they typically showed hysteresis due to a non-linear effect that was observed and discussed in our previous measurements on quartz microfibers [30], and also in a paper whose focus was parametric resonances in B nanowires [31].

During electrical excitation, the applied force acting on the cantilevered conductive nanowire is a function of the external electric field and its frequency [19,20]. Typically an ac signal ( $V_{ac}\cos\omega t$ ) with dc bias ( $V_{dc}$ ) is applied between the two electrodes. The force acting on the nanowire is:

$$\begin{aligned}
 F(t) &= a(\Delta V + V_{dc} + V_{ac}\cos\omega t)^2 \\
 &= a(\Delta V + V_{dc})^2 + \frac{1}{2}aV_{ac}^2 + 2a(\Delta V + V_{dc})V_{ac} \\
 &\quad \times \cos\omega t + \frac{aV_{ac}^2}{2}\cos 2\omega t,
 \end{aligned} \quad (3)$$

where  $\Delta V$  is the static potential to balance the work function difference between the two electrodes [19,20], and  $a$  is a proportionality constant. Eq. (3) shows that the force,  $F(t)$ , contains  $\omega$  and  $2\omega$  components. If the linear term ( $\cos\omega t$ ) dominates the beam resonance, the driving frequency equals the nanowire's resonance frequency. If the quadratic term ( $\cos 2\omega t$ ) dominates the resonance, the driving fre-

quency is only one half the nanowire's resonance frequency. To ensure the correct assignment of the nanowire's resonance frequency, the response of each nanowire was examined at excitation frequencies around one half and double the measured resonance frequency. Most of the nanowires were also mechanically excited during the same experimental session, which enabled the direct comparison between the two excitation methods and ensured the determination of the true resonance frequency.

The driving force for mechanical excitation is generated by the mechanical vibration of the piezoelectric bender as a result of an applied ac voltage; the excitation envelope is thus governed by the frequency response of the piezoelectric bender. According to our measurement, the cantilevered piezoelectric bender ( $15 \times 8 \times 0.8 \text{ mm}^3$ ) had a resonance frequency of  $\sim 327.7 \text{ Hz}$  and a quality factor of 13 in the SEM vacuum chamber. The resonance frequencies of the cantilevered B nanowires were typically on the order of hundreds of kilohertz, which is much higher than the resonance frequency of the piezoelectric bender. The applied ac signal with an approximately several hundred kilohertz frequency is far off the resonance of the piezoelectric bender, and thus does not generate a large mechanical excitation. We have found that with our current setup the mechanical excitation method is most effective for frequencies lower than 500 kHz. In contrast, for the electrical excitation method, the strength of the electric field does not depend on the frequency of the ac signal. Therefore, the electrical excitation method works well for any frequency the function generator can supply. However, the introduction of an additional electric field in the SEM degrades the imaging quality, which worsens with increasing magnitude of the electric field. Therefore, electrical excitation is not suitable for high stiffness nanostructures that require a strong electric field but have a small vibration amplitude.

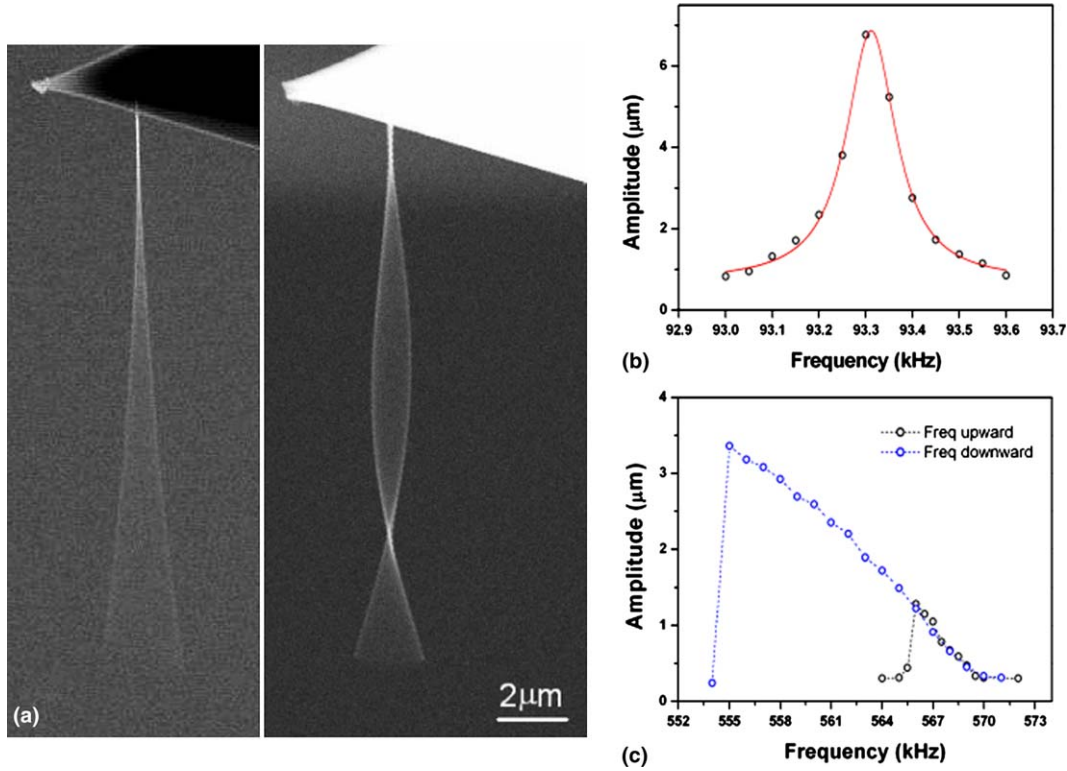


Fig. 3. (a) SEM images of the first (left) and second (right) resonance modes of a cantilevered B nanowire. (b) Typical amplitude–frequency response curve of the first resonance mode of a B nanowire with a Lorentzian fit (solid line). (c) Typical amplitude–frequency response curve of the second resonance mode of a B nanowire.

The geometry of each nanowire was measured in the SEM. The diameters of nanowires were measured before the test, and verified after the test. SEM images only provide a two-dimensional (2D) projection of the nanowire, thus care must be taken when measuring the nanowire’s length. In Eq. (1) the bending modulus is proportional to the beam length to the fourth power. Thus any error in the measured length,  $\Delta L$ , translates into a relative error in the final value of the bending modulus of  $4\Delta L/L$ . In an effort to accurately measure the length, the nanowire was measured again in the SEM after each resonance test. The AFM cantilever with the B nanowire still attached was directly mounted on a conventional SEM holder. Images of the nanowire were acquired at two angles: with the SEM holder normal to the electron beam and at a tilt angle of 45°. A parallax method was used to reconstruct a three-dimensional representation of the nanowire based on these two SEM images [32]. The lengths of all the nanowires reported in this study were obtained using this method.

Boron can be oxidized in air at room temperature, and oxide layers on boron particles [17] and nanoribbons [33] have been observed. An amorphous oxide coating was found on the surface of these B nanowires by TEM (Fig. 4(a)). Since the physical properties of boron oxide are different from those of pure boron, it is important to analyze the effect of the oxide layer on resonance so as to get the bending modulus of the boron core.

As shown in Eq. (2), for a constant diameter circular cross-section beam, the Young’s modulus can be calculated from the resonance frequency and geometry:

$$E_{\text{beam}} = \frac{64\pi^2 \rho L^4}{\beta_n^4 D^2} f_n^2. \quad (4)$$

For a B nanowire of diameter  $D$  with an oxide layer thickness  $T$ , the resonance frequency is

$$\begin{aligned} f_n &= \frac{\beta_n^2}{2\pi} \frac{1}{L^2} \sqrt{\frac{E_B I_B + E_O I_O}{\rho_B A_B + \rho_O A_O}} \\ &= \frac{\beta_n^2}{8\pi} \frac{1}{L^2} \sqrt{\frac{(E_B - E_O)(D - 2T)^4 + E_O D^4}{(\rho_B - \rho_O)(D - 2T)^2 + \rho_O D^2}}, \end{aligned} \quad (5)$$

where  $E_B$  and  $E_O$  are the Young’s moduli of the boron and boron oxide ( $B_2O_3$ ), and  $\rho_B$  and  $\rho_O$  are the densities of the boron and boron oxide, respectively. Introducing a ratio parameter  $\gamma = \frac{D-2T}{D}$ , the Young’s modulus of boron can be obtained from Eq. (5) as follow:

$$E_B = \frac{64\pi^2}{\beta_n^4} \frac{L^4}{\gamma^2 D^2} \left( \rho_B + \rho_O \left( \frac{1}{\gamma^2} - 1 \right) \right) f_n^2 + E_O \left( 1 - \frac{1}{\gamma^4} \right). \quad (6)$$

Inserting the beam modulus expression (Eq. (4)) into the boron modulus expression (Eq. (6)), we have the following relationship:

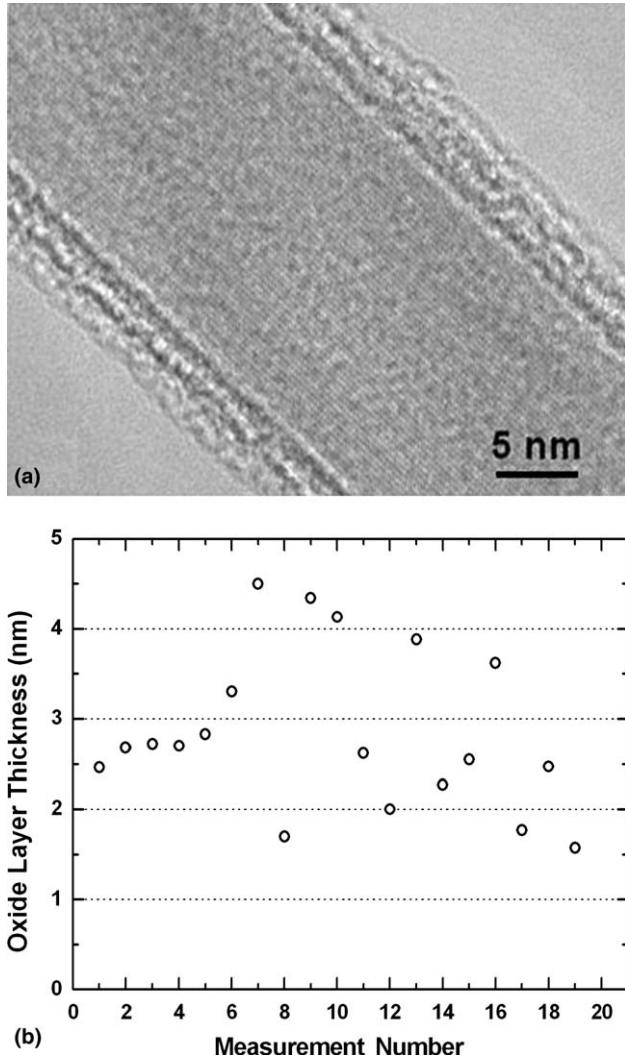


Fig. 4. (a) TEM image of a B nanowire with an amorphous oxide layer; (b) oxide layer thickness measured inside TEM.

$$E_B = \frac{1}{\gamma^2} \left( 1 + \frac{\rho_O}{\rho_B} \left( \frac{1}{\gamma^2} - 1 \right) \right) E_{\text{beam}} + E_O \left( 1 - \frac{1}{\gamma^4} \right). \quad (7)$$

The Young's modulus of boron ( $E_B$ ) can thus be obtained from the fit value for  $E_{\text{beam}}$ .

### 3.3. Resonance test results

Crystalline boron has several polymorphs:  $\alpha$ -rhombohedral,  $\alpha$ -tetragonal, and  $\beta$ -rhombohedral. The densities of  $\alpha$ -rhombohedral and  $\beta$ -rhombohedral boron are  $2.45 \times 10^3 \text{ kg/m}^3$  and  $2.35 \times 10^3 \text{ kg/m}^3$ , respectively [34]. The Young's modulus for  $\beta$ -rhombohedral boron crystal is  $\sim 400 \text{ GPa}$  [16]. To the best of our knowledge there is no report of the modulus of  $\alpha$ -rhombohedral boron. An average density of  $2.4 \times 10^3 \text{ kg/m}^3$  was used for the boron core. TEM electron-diffraction of the B nanowires used in this study indicates a crystal structure that does not match any of the known crystalline phases of boron. An orthorhombic unit cell with  $a = 9.4 \text{ \AA}$ ,  $b = 7.1 \text{ \AA}$ , and  $c = 5.4 \text{ \AA}$  was consistent with nanodiffraction data [18]. If we

make the assumption that this new crystalline phase is a distorted  $\alpha$ -tetragonal structure [35], there would be 50 atoms per unit cell and accounting for the volume of the unit cell [18] the calculated density would be  $2.5 \times 10^3 \text{ kg/m}^3$ ; the density of  $\alpha$ -tetragonal B is  $2.31 \times 10^3 \text{ kg/m}^3$  [36]. The density of amorphous boron oxide ( $\text{B}_2\text{O}_3$ ) is  $1.80 \times 10^3 \text{ kg/m}^3$  [37], and its Young's modulus is  $\sim 16 \text{ GPa}$  [37].

As indicated in Eq. (5), the thickness of the oxide layer is needed to correct the measured Young's modulus. Measuring the thickness of the oxide layer could only be done in the TEM. However, transferring nanowires attached to AFM cantilevers into a TEM is challenging due to limitations on the specimen size. Instead, we measured the oxide thickness for B nanowires from the same source that were not tested. Fig. 4(b) shows the oxide layer thickness measurement results performed in a Hitachi HF-2000 TEM. The average oxide layer thickness was  $\sim 3 \text{ nm}$  and this value was used in the data analysis.

With the measured resonance frequency and the nanowire geometry, the bending modulus of each nanowire was first calculated without accounting for the oxide layer. Corrections were then made to the modulus results according to Eq. (7). The corrected bending modulus values for the B nanowires are listed in Table 1.

The average bending modulus of boron from our resonance measurements is  $\sim 310 \text{ GPa}$ , which is lower than the Young's modulus of bulk  $\beta$ -rhombohedral boron [16]. This might be due to the fact that these B nanowires have a different crystal structure. The assumptions made in our data analysis about boron density and oxide layer thickness may also contribute to the difference. Another factor that bears attention is a non-ideal boundary condition.

### 3.4. Boundary conditions

The resonance method has been used by several researchers to measure the mechanical properties of nanostructures [19–22,30]. The analysis of mechanical resonance tests is based on simple beam theory. According to beam theory, the fixed end boundary condition requires zero displacement and slope at the fixed end. The 'fixed' end of the nanostructure is typically assumed to be perfectly clamped. To test this issue, we performed a series of tests to investigate the effect of the clamp on the resonance frequency of cantilevered nanowires.

Table 1  
Bending modulus of boron nanowires from mechanical resonance tests

Length ( $\mu\text{m}$ )	Diameter (nm)	Frequency (kHz)	Bending modulus (GPa)
$8.8 \pm 0.2$	$43 \pm 2$	$670.7 \pm 0.05$	$300 \pm 48$
$17.8 \pm 0.2$	$68 \pm 2$	$288.0 \pm 0.05$	$310 \pm 22$
$16.2 \pm 0.2$	$74 \pm 2$	$387.7 \pm 0.05$	$310 \pm 26$
$35.1 \pm 0.2$	$77 \pm 2$	$93.3 \pm 0.05$	$370 \pm 22$
$20.0 \pm 0.2$	$52 \pm 2$	$163.0 \pm 0.05$	$300 \pm 32$
$13.6 \pm 0.2$	$48 \pm 2$	$303.8 \pm 0.05$	$270 \pm 34$
$6.4 \pm 0.1$	$80 \pm 2$	$2920.7 \pm 0.05$	$350 \pm 31$
$56.5 \pm 0.4$	$95 \pm 2$	$49.8 \pm 0.05$	$410 \pm 24$

In this study EBID was used in an effort to ensure that true fixed-end boundary conditions were met. In EBID, material is deposited onto a substrate by irradiation with an electron beam. It has been used to fabricate nanoscale clamps in situ inside a SEM [21,27,38,39]. In the EBID process the secondary electrons decompose molecules that have adsorbed on the substrate surface or are present in a gas phase near the surface; these molecules can be either precursor gas molecules deliberately introduced, or residual hydrocarbon molecules from the pump oil of the vacuum system. Decomposition of these molecules leads to the formation of a deposit on the substrate surface. EBID deposits were used to attach each B nanowire tested to the AFM cantilever tip (Fig. 5(a)).

As introduced previously, the nanowire source was prepared in such a way that B nanowires were attached to the edge of a TEM grid section without any mechanical clamp (Fig. 1(b)). These protruding nanowires were good candi-

dates to investigate the effect of boundary conditions since they provided an opportunity to easily alter the boundary conditions. In two cases B nanowires were picked up with an AFM tip without depositing an EBID clamp. These nanowires were also used to study the resonance with and without the EBID clamp.

The process used to test the effect of boundary conditions is as follows. First, the resonance frequency of a naturally clamped (held only by adhesion forces) B nanowire was measured. A short period exposure to the electron beam (~5 min) was then performed to EBID deposit a small amount of carbonaceous material onto the AFM tip substrate to attach the nanowire. The resonance frequency of the nanowire was then measured again. The process of depositing more material was then repeated by EBID (in the same region) several times and the resonance frequency was measured after each deposition. We found that the resonance frequency increased after each addi-

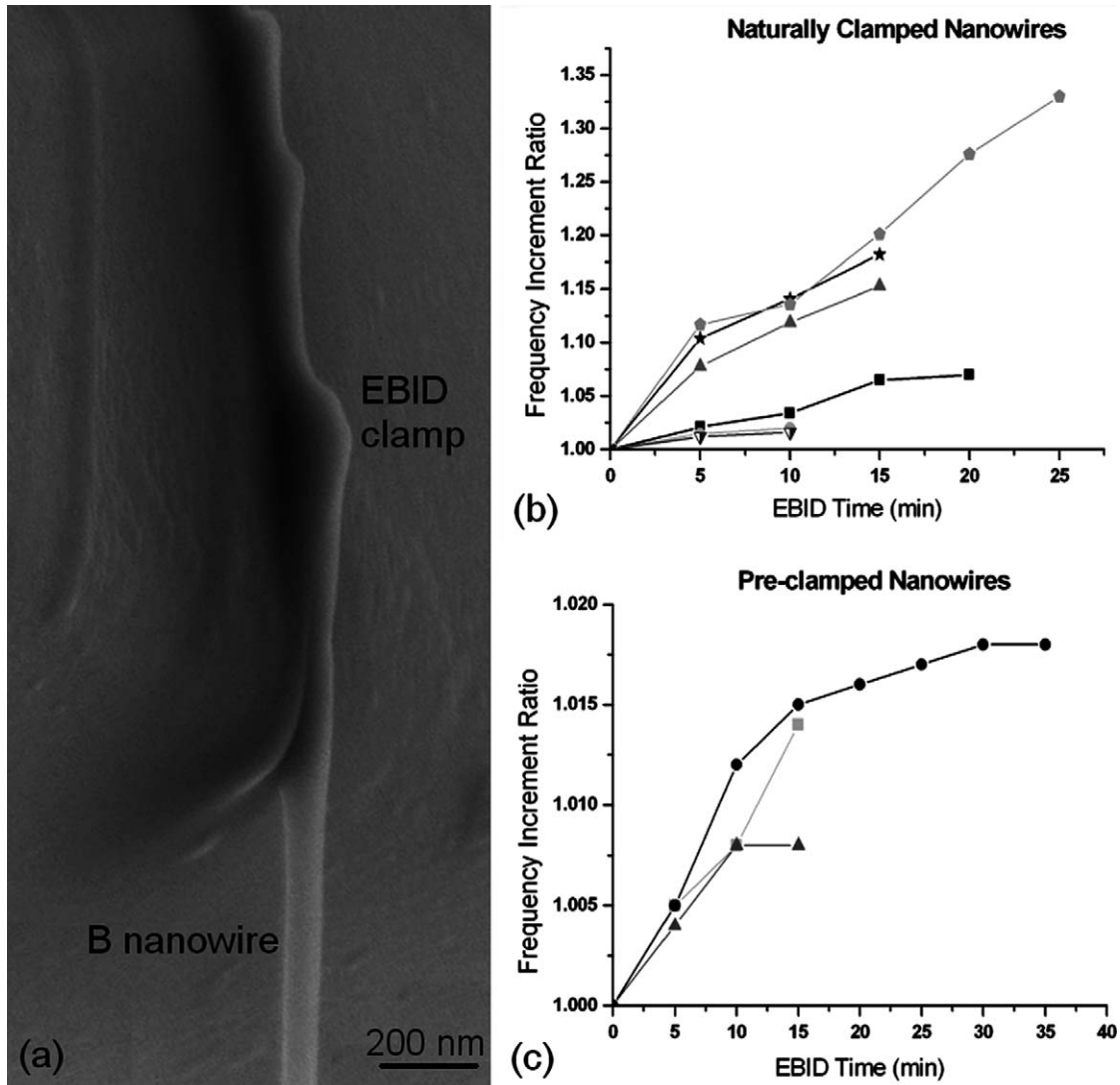


Fig. 5. (a) SEM image of a B nanowire being clamped to an AFM tip surface with EBID method. (b) Frequency increment ratio after each EBID clamping for six B nanowires that were initially held without EBID clamping. (c) Frequency increment ratio for three pre-clamped B nanowires.

tional EBID deposit was added, eventually approaching a plateau (Fig. 5(b)). Due to the allowed time for an experiment session, there were a few cases where the resonance frequency did not reach a plateau. The overall resonance frequency change for the six B nanowires tested in this manner ranged from 1.7 to 25 percent.

While it is tempting to conclude that having a stronger attachment leads to an increase of the resonance frequency, it is possible that the frequency increase is caused by a decrease of the effective beam length due to the build up of EBID material. Assuming perfect boundary conditions, the length decrease required to cause the measured frequency shift was calculated and was found to be much larger than the clamp length. The EBID clamps were always fabricated at the edge of the substrate so as to obtain a well-defined cantilevered length  $L$ . It is difficult to define the original cantilevered length for a protruding nanowire naturally attached to the substrate. However, after the first (small) EBID deposit (perhaps thus fixing  $L$ ), and relative to the final deposit, there is often still a significant change in frequency (see Fig. 5(b)). These experiments clearly demonstrate that non-ideal boundary conditions can lead to a lower resonance frequency than a more perfectly clamped case.

Most of the nanowires tested in this study were clamped to an AFM tip with the EBID method before being picked up from the source. This EBID process typically took 30 min with a deposition thickness of  $\sim 30$  nm. These EBID clamps were strong enough to survive the process of pulling the nanowires away from the source, however, it is still possible that the clamps were not as perfect as required by beam theory.

To further test the dependence of the measured frequency on the clamp type we measured the resonance frequency after each deposition (for several sequential EBID deposits) of three previously clamped and tested B nanowires. A slight increase (less than 2%) in the resonance frequency was observed before a stable value was reached (Fig. 5(c)). Compared with the non-clamped nanowires, these pre-clamped nanowires clearly have boundary conditions that better approximate the ideal fixed end boundary condition. Therefore, it is reasonable to conclude that the resonance frequencies reported in Table 1 are very close to, but may be slightly less, than the resonance frequencies of perfectly clamped nanowires.

## 4. Nanoscale tensile testing

### 4.1. Tensile test experimental setup

Tensile tests were also performed on the crystalline B nanowires using our home-made nanomanipulator inside the LEO 1525 SEM. Two AFM cantilever chips were mounted on the two opposing positioning stages. Soft cantilevers (Chip NSC 12, length 350 and 300  $\mu\text{m}$ , nominal force constant 0.30 and 0.35 N/m, respectively, Mikro-Masch, Inc.) were mounted on the  $X$ - $Y$  linear motion

stage, and rigid cantilevers (Chip NSC 12, length 90 and 110  $\mu\text{m}$ , nominal force constant 14.0 and 7.5 N/m, respectively, MikroMasch Inc.) were mounted on the  $Z$  linear motion stage together with the B nanowire source. The force constants of the cantilevers were calibrated in situ prior to the tensile test using the resonance method developed by Sader et al. [40]. The resonance frequencies and dimensions of the cantilevers were measured in the SEM allowing the cantilever force constants to be calculated. A detailed description of the calibration procedure has been reported elsewhere [38].

During a typical tensile test, an individual B nanowire was picked up from the source and clamped to two opposing AFM tips (Fig. 6). The clamps were formed with our recently developed and quite rapid EBID method [29]. The soft cantilever was then gradually moved away from the rigid cantilever by actuating the piezoelectric bender with a dc voltage. A continuously increasing tensile load was applied to the nanowire until fracture. We currently do not have any means to directly record the tensile load

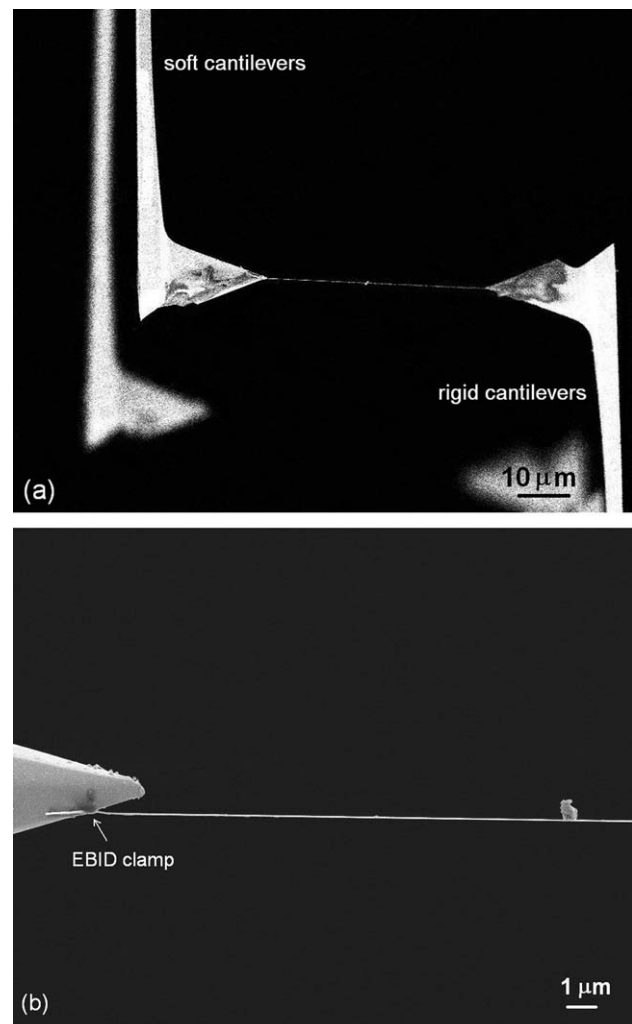


Fig. 6. (a) A B nanowire clamped between two AFM cantilever tips under a tensile load. (b) A high magnification SEM image showing a portion of a B nanowire under tension.

or strain during the test, so we relied on image analysis of a series of SEM images taken during the tensile loading process. We also measured the nanowire diameter by SEM.

Since we must rely on image analysis to obtain the tensile load and strain, proper specimen alignment is critical. The SEM provides a projected two-dimensional image. To get an accurate length the entire nanowire needs to be in the projection plane. This is achieved by carefully adjusting the heights of the two ends of the nanowire using  $Z$  linear motion until both ends are in focus before final clamping. However, because SEM has a large depth of focus and therefore poor  $Z$ -resolution, a slight height mismatch between the two ends of the nanowire may still exist even though they both 'seem to be in focus'. A method for obtaining the correct length is used, as discussed below.

#### 4.2. Tensile test data analysis

The tensile loading process was recorded in a series of SEM images taken during the test. From these images the length of the nanowire at each load was measured. In some cases, small particles that were stuck to the nanowire along the gauge length served as reference points for higher magnification measurement of length along certain segments (Fig. 6(b)). The nanowire length was obtained by counting the number of pixels in the SEM image, which determines the strain resolution. The recorded SEM images have a resolution of  $1024 \times 768$  pixels, and a nanowire typically spans less than 1000 pixels in the image. Also, with the deflection of the cantilever the nanowire gradually changes its orientation, making it difficult to implement interpolation algorithms used to achieve sub-pixel displacement resolution [41]. Therefore, the nanowire length was measured with a resolution of one pixel and thus a strain resolution of 0.1–0.2%.

The AFM cantilever serves as the force-sensing element and the applied tensile force is obtained by measuring the cantilever deflection and multiplying it by the cantilever force constant. However, the direct measurement of the cantilever deflection over the entire experiment is challenging due to a lack of an internal reference point. The force-sensing cantilever used here was 300 or 350  $\mu\text{m}$  in length, but in most cases the maximum deflection at the tip was only  $\sim 10 \mu\text{m}$ . So using the fixed end of the cantilever as the reference for the tip's deflection yields poor resolution. One alternative is to use a nearby unloaded cantilever tip as a reference, but the resolution is limited because the nearby AFM tip is not in focus (Fig. 6(a)). Instead of directly measuring the cantilever deflection, we employed two other methods to calculate the deflection: (1) by measuring the cantilever deflection angle and (2) by calibrating the piezoelectric bender response.

For a tip-loaded cantilever, the deflection ( $\delta$ ) and angle of deflection ( $\theta$ ) at the cantilever tip are given by:  $\delta = \frac{PL^3}{3EI}$  and  $\theta = \frac{PL^2}{2EI}$ . Here  $P$  is the load applied at the tip,  $L$  is the cantilever length,  $E$  is the elastic modulus and  $I$  is the moment of inertia of the cantilever. The cantilever deflec-

tion can be represented by the angle of deflection with the following relationship:

$$\delta = \frac{2}{3}\theta L. \quad (8)$$

In all the tensile tests the maximum cantilever deflection was less than five percent of the cantilever's length. So the cantilever deflection is within the linear regime and the equations presented above are valid. Since no reference point is needed to measure the deflection angle, high-resolution images can be taken for accurate angle measurement and the corresponding cantilever deflection can be thereby determined.

The second technique used to calculate the cantilever deflection was through the calibration of the response of the piezoelectric bender to an applied dc voltage. As previously discussed, the tensile load was applied through the bending of the piezoelectric bender in response to the applied dc voltage. During the tensile experiment, the applied dc voltage corresponding to each SEM image was recorded. After the test, the same voltage was applied to the piezoelectric bender, and the displacement of the unloaded cantilever was recorded. The difference between the displacements of the unloaded and loaded cantilever is the corresponding cantilever deflection at that specific loading step [42]. The cantilever deflections obtained based on these two methods agree within ten percent. The piezoelectric bender response calibration method was employed to obtain the cantilever deflection in all of the results reported here.

As previously discussed, in some cases the nanowire being tested is not perfectly aligned with the axis of the applied load. Li et al. studied the effect of tensile offset angle on micro/nanoscale tensile testing [43]. The tensile offset angle of a tensile loaded microfiber was monitored with two CCD imaging systems that provided front and side views. Our tensile loading experiments were performed in a SEM that provides only a top view of the nanostructure. Thus, we can only monitor the misalignment in the  $X$ - $Y$  plane but cannot detect slight height mismatch in the  $Z$ -direction. Fig. 7 shows schematics of both in-plane misalignment and height mismatch arising from the angles  $\alpha$  and  $\beta$ , respectively (Fig. 7(c)). Please note that both angles gradually change with increasing tensile load.

For the purpose of analysis the tensile load,  $F$ , is decomposed into three components:  $F_x$ ,  $F_y$  and  $F_z$ , leading to the following relationships:

$$\begin{aligned} F_y &= F_x \tan \alpha \\ F_z &= F_{xy} \tan \beta = F_x \tan \beta \sqrt{1 + \tan^2 \alpha}. \end{aligned} \quad (9)$$

Here  $F_y$  and  $F_z$  are written in terms of  $F_x$  because it is the major force component causing cantilever deflection. Fig. 7(a) indicates that the measured cantilever deflection is caused by a combination of the  $F_x$  and  $F_y$  force components:

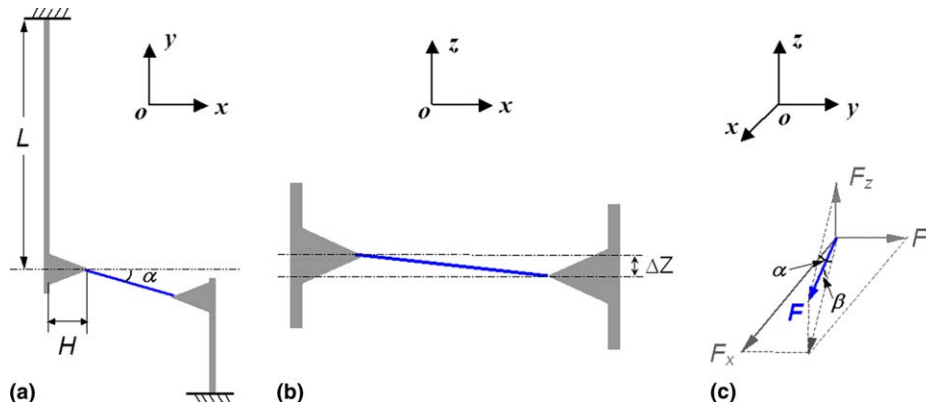


Fig. 7. (a) Top view of the tensile test setup with misalignment in the  $X$ - $Y$  plane; (b) side view of the tensile test setup with a height mismatch; (c) decomposition of the tensile load.

$$k\Delta x = F_x - F_y \frac{H}{L}, \quad (10)$$

where  $k$  is the cantilever force constant,  $\Delta x$  is the cantilever deflection,  $H$  is the distance from the clamped end of the nanowire to the central plane of the cantilever, and  $L$  is the cantilever length. The force  $F_y$ , acting on the cantilever has a negligible effect. The relationship between the total tensile load,  $F$ , acting on the nanowire and the AFM cantilever deflection,  $\Delta x$ , can be obtained by combining Eqs. (9) and (10) as follows:

$$\begin{aligned} F &= \sqrt{F_x^2 + F_y^2 + F_z^2} \\ &= F_x \sqrt{1 + \tan^2 \alpha + \tan^2 \beta + \tan^2 \alpha \tan^2 \beta} \\ &= \frac{k\Delta x}{1 - \frac{H}{L} \tan \alpha} \sqrt{1 + \tan^2 \alpha + \tan^2 \beta + \tan^2 \alpha \tan^2 \beta} \quad (11) \end{aligned}$$

The height mismatch (if present) affects both the calculated tensile load and strain. Since we are not able to measure the height mismatch between the two ends of a nanowire in situ in the SEM, the force in the  $X$ - $Y$  plane,  $F_{xy}$ , is assumed to be the total force, given by

$$F_{xy} = \sqrt{F_x^2 + F_y^2} = F \cos \beta. \quad (12)$$

So a height mismatch leads to an error of  $1 - \cos \beta$  in measured force. For a given height mismatch, the longer the nanowire, the smaller the angle  $\beta$  and the smaller error in measured force. With respect to the measured values of strain, the SEM images only provide the projected elongation, which is not the true elongation, as shown in Fig. 8. For a nanostructure of length  $L$  with a height mismatch  $\Delta Z$ , the measured strain for a true strain of  $\frac{\Delta L}{L}$  is:  $\frac{\sqrt{(L+\Delta L)^2 - (\Delta Z)^2} - \sqrt{L^2 - (\Delta Z)^2}}{\sqrt{L^2 - (\Delta Z)^2}}$ . For any nonzero height mismatch, we have the following relationship:

$$\frac{\sqrt{(L + \Delta L)^2 - (\Delta Z)^2} - \sqrt{L^2 - (\Delta Z)^2}}{\sqrt{L^2 - (\Delta Z)^2}} > \frac{\Delta L}{L}, \quad (13)$$

which indicates that the strain measured in the SEM is always larger than the true strain in the nanowire.

Any height mismatch (that is not corrected for) between the two ends of a nanowire in our tensile experiments leads to a lower measured tensile load and a higher measured strain, which consequently results in lower values for the tensile strength and Young's modulus. It is desirable to eliminate the height mismatch during the experiment, but due to the poor  $Z$ -resolution of the SEM it is intrinsically not possible to detect a small height mismatch between the two ends of a nanowire. Following each tensile test, the AFM tip with a nanowire fragment attached was imaged in the SEM, and the misalignment angle  $\beta$  was measured by assuming the nanowire returned to its initial orientation following fracture. The height mismatch was then calculated, and the tensile load and strain measurements were corrected using the procedure described above. The height mismatch caused errors of roughly 5% (tensile load) and 10% (strain) in our measurements.

As in the resonance test data analysis, a correction is needed to account for the boron oxide layer in order to get the tensile strength and Young's modulus of the boron core. In an effort to simplify the data analysis, two assumptions were made: First, the boron core and oxide layer share the same strain while in tension (strain identical condition is assumed). This is reasonable because we never saw any delamination of the oxide layer at the fracture surface, indicating a strong interaction between the boron core and oxide coating. Second, at the moment of fracture the stress in the oxide layer is below its fracture strength. This assumption is necessary because to the best of our knowledge there is no experimental data on the fracture strength of boron oxide. For confirmation, we calculated the maximum tensile stress in the oxide layer at the time of fracture for each of the nanowires measured. The maximum tensile stresses ranged from 150 to 500 MPa, which does not seem to invalidate this assumption.

Based on these assumptions, a B nanowire of diameter  $D$  (oxide layer thickness  $T$  included) with an applied load of  $F$  and corresponding strain of  $\varepsilon$ , without considering

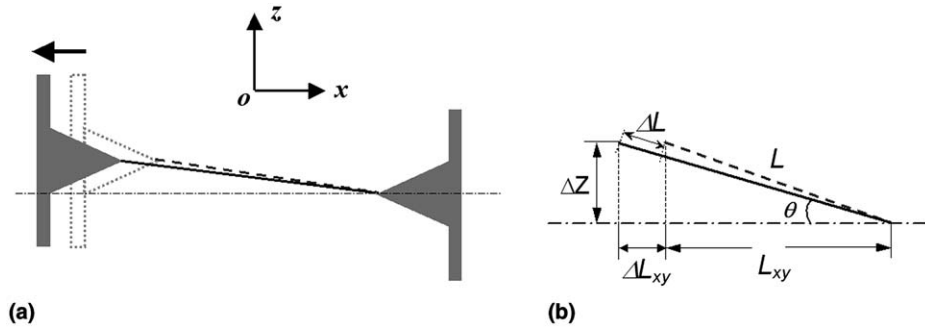


Fig. 8. (a) Side view of nanowire elongation in the presence of a non-zero height mismatch; (b) schematic showing the elongation of the projected length and true length in the presence of a height mismatch.

oxide layer, has the following relationship for the internal stress:

$$F = \sigma_{\text{beam}} \frac{\pi}{4} D^2. \tag{14}$$

Considering the oxide layer, the modified relationship has the following form:

$$F = \sigma_B \frac{\pi}{4} (D - 2T)^2 + E_o \varepsilon \frac{\pi}{4} (D^2 - (D - 2T)^2). \tag{15}$$

Here  $\sigma_{\text{beam}}$  is the tensile stress in the entire nanowire (average tensile stress),  $\sigma_B$  is the tensile stress in the boron core, and  $E_o$  is the Young's modulus of boron oxide. Again using the parameter  $\gamma = \frac{D-2T}{D}$ , the true stress in the boron core can be expressed as:

$$\sigma_B = \frac{\sigma_{\text{beam}}}{\gamma^2} + E_o \varepsilon \left( 1 - \frac{1}{\gamma^2} \right). \tag{16}$$

Thus the true stress in boron core can be obtained from the average tensile stress in the nanowire.

No correction is needed for the Young's modulus because the modulus is obtained from linear fitting of the stress–strain curve. With the corrected tensile stress values, the Young's modulus of the boron core can be obtained.

### 4.3. Tensile test results

Tensile tests were performed on nine B nanowires. The cantilever deflection and nanowire elongation were obtained from image analysis, and the corresponding tensile load and strain were calculated. Following each experiment, the nanowire fragments were observed in the SEM, and the misalignment angle was obtained. The corresponding height mismatch was then calculated, and corrections were made to the previously calculated tensile load and strain. With nanowire diameter measurement, the corresponding tensile stress (average tensile stress) was calculated. Assuming a uniform 3 nm boron oxide layer with a Young's modulus of 16 GPa, corrections were made on the tensile stress to obtain the true stress in the boron core.

With the corrected stress and strain values, a stress–strain diagram was plotted. Fig. 9(a) shows a stress–strain relationship for a B nanowire under tension; through data fitting, the

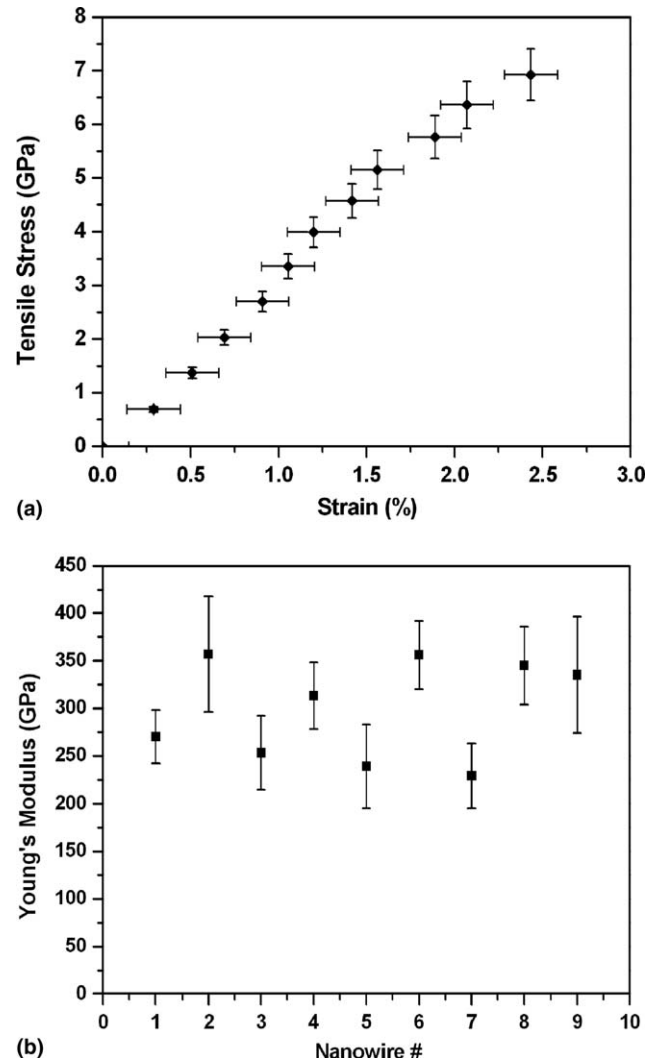


Fig. 9. (a) The stress–strain relationship of a B nanowire under tension. (b) The Young's modulus results from tensile test.

Young's modulus (the slope of the stress–strain curve) was obtained. The tensile testing results on nine B nanowires are listed in Table 2, and the Young's modulus data is shown in Fig. 9(b). The Young's modulus values obtained from the tensile tests are in reasonable agreement with the results from the mechanical resonance test. It is important to note that 7

Table 2  
Tensile test results of boron nanowires

Length ( $\mu\text{m}$ )	Diameter (nm)	Maximum strain (%)	Fracture strength <sup>a</sup> (GPa)	Young's modulus <sup>b</sup> (GPa)
$66.5 \pm 0.02$	$48 \pm 2$	$1.6 \pm 0.1$	$4.5 \pm 0.5$	$270 \pm 28$
$13.8 \pm 0.02$	$42 \pm 2$	$1.4 \pm 0.1$	$5.0 \pm 0.6$	$360 \pm 61$
$7.9 \pm 0.02$	$40 \pm 2$	$2.5 \pm 0.1$	$6.4 \pm 0.8$	$250 \pm 39$
$44.9 \pm 0.02$	$48 \pm 2$	$2.0 \pm 0.1$	$5.9 \pm 0.6$	$310 \pm 35$
$7.5 \pm 0.02$	$50 \pm 2$	$1.7 \pm 0.1$	$4.1 \pm 0.6$	$240 \pm 44$
$45.5 \pm 0.02$	$50 \pm 2$	$2.4 \pm 0.1$	$7.5 \pm 0.8$	$360 \pm 36$
$25.4 \pm 0.02$	$58 \pm 2$	$1.1 \pm 0.1$	$2.2 \pm 0.2$	$230 \pm 34$
$23.0 \pm 0.02$	$44 \pm 2$	$2.9 \pm 0.1$	$8.2 \pm 1.0$	$350 \pm 41$
$23.3 \pm 0.02$	$46 \pm 2$	$1.0 \pm 0.1$	$3.5 \pm 0.4$	$340 \pm 61$

<sup>a</sup> B nanowires 3–9 broke at the clamp; B nanowires 1 and 2 broke near one clamp (within a few microns).

<sup>b</sup> The value (0,0) was included in the fit of Young's modulus.

of the B nanowires failed essentially at one of the clamps, and the other two within a few microns of one of the clamps. Consequently, these values should be considered as lower bounds to the fracture strength of such nanowires. A future challenge will be configuring experiments on such nanowires so

that the complicating factor of stress concentration near a clamp is overcome.

Fig. 10 presents the nanowire fracture strength versus the nanowire length (Fig. 10(a)) and diameter (Fig. 10(b)). Given that there are only nine strength values, it is perhaps not surprising that there is no obvious functional relationship between strength and either length or diameter. A much larger dataset is needed to treat the statistics of fracture of such B nanowires. A further complicating factor is failure near or at one of the EBID clamps, as mentioned above.

Larger diameter boron fibers have been made and studied [44–49]. The fibers are made by a thermal CVD process [44,45] in which  $\text{BBr}_3(\text{g})$  or  $\text{BCl}_3(\text{g})$  is reduced by hydrogen at high temperature and boron is deposited onto a tungsten filament, diffuses into the filament and transforms it into a core consisting of a polycrystalline mixture of tungsten borides; amorphous or crystalline B then surrounds this core and the fiber diameter (typically hundreds of microns in diameter) is determined by the CVD growth conditions. A detailed review of B fiber preparation is provided in Ref. [50]. The mechanical properties of B fibers have been intensively studied by tensile testing and they show brittle fracture with tensile strengths in the range of 2–5 GPa [44,46–49] and elastic modulus values from 390 to 440 GPa.

Many experimental studies have been conducted to investigate the relationship between B fiber structure and fracture strength [46–49]. For example, Carlsson [49] studied the relationship between fiber morphology and mechanical properties for B fibers fabricated in the temperature range 1000–1500 °C. He classified the B fibers into two main categories: amorphous fibers and crystalline fibers. Three different amorphous nodule morphologies were identified with different mechanical properties: amorphous B fibers with nodules radially aligned along the tungsten filament were found to possess the highest fracture strength ( $\sim 3.3$  GPa). Amorphous B fibers with uneven amorphous nodules had an average fracture strength  $\sim 2.5$  GPa. Amorphous B fibers with randomly oriented nodules on top of a crystalline boron layer had lower fracture strength ( $< 1.5$  GPa). The B fibers with a crystalline morphology were found to have the lowest fracture strength ( $< 1$  GPa). Carlsson concluded that having an

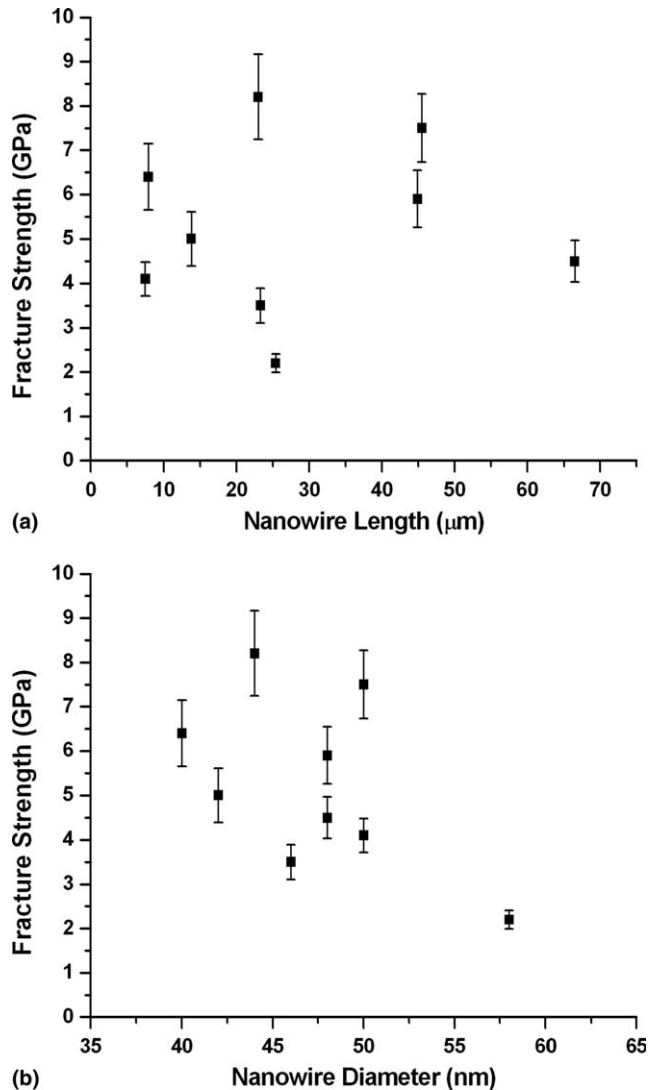


Fig. 10. B nanowire fracture strength as a function of (a) nanowire length and (b) nanowire diameter.

amorphous mantle would provide the highest fracture strength. Carlsson and coworker [48] also investigated the influence of strain-rate, gauge length and fiber diameter on the tensile fracture strength of B fibers. They found that the fracture strength of the B fibers tested was independent of the strain-rate as well as the fiber diameter but decreased with an increase of the gauge length.

Because of their excellent mechanical properties, B fibers have been used as high-performance reinforcement in advanced composites [51,52]. Perhaps the high modulus, high-strength B nanowires (having also a large aspect ratio) discussed herein will figure prominently in future advanced ceramic and metal matrix composites.

## 5. Conclusion

Crystalline boron nanowires were studied with a mechanical resonance method inside a SEM. The mechanical resonance of cantilevered nanowires was excited with an electrically or mechanically induced periodic load. The nanowire's diameter was measured in the SEM, and a three-dimensional reconstruction method was used to obtain the nanowire length. An oxide layer on the surface of the nanowires was observed by TEM. A correction was made to the resonance test results to account for the influence of the boron oxide coating. The Young's modulus values obtained ranged from 300 to 400 GPa. The effect of boundary conditions on the resonance frequency was studied and imperfect clamping was found to reduce the resonance frequency of the cantilevered nanowire.

Tensile tests were also performed on the boron nanowires, and the fracture strength and Young's modulus values were obtained. The fracture strength of the nine B nanowires tested ranged from 2 to 8 GPa. The average elastic modulus obtained with the tensile tests is  $\sim 320$  GPa, consistent with the resonance test results.

## Acknowledgments

This work was funded by NSF EEC-0210120, and in part by ONR #N000140210870 (partial support, W. Ding) and by the NASA BIMat URETI # NCC-1-02037 (support for X Chen). The SEM and TEM work was performed in the EPIC facility of NUANCE Center at Northwestern University. The NUANCE Center is supported by NSF-NSEC, NSF-MRSEC, Keck Foundation, the State of Illinois, and Northwestern University. We appreciate receiving the boron nanowires from C. Otten (Buhro group, Washington University, St. Louis).

## References

- [1] Star A, Han TR, Joshi V, Gabriel JCP, Gruner G. Nanoelectronic carbon dioxide sensors. *Adv Mater* 2004;16(22):2049–52.
- [2] Wongwiriyan W, Honda SI, Konishi H, Mizuta T, Ikuno T, Ito T, et al. Single-walled carbon nanotube thin-film sensor for ultrasensitive gas detection. *J Jpn Appl Phys Lett* 2005;44(16–19):L482–4.
- [3] Schadler LS, Giannaris SC, Ajayan PM. Load transfer in carbon nanotube epoxy composites. *Appl Phys Lett* 1998;73(26):3842–4.
- [4] Qian D, Dickey EC, Andrews R, Rantell T. Load transfer and deformation mechanisms in carbon nanotube-polystyrene composites. *Appl Phys Lett* 2000;76(20):2868–70.
- [5] Thostenson ET, Chou TW. Aligned multi-walled carbon nanotube-reinforced composites: processing and mechanical characterization. *J Phys D* 2002;35(16):L77–80.
- [6] Dalmas F, Chazeau L, Gauthier C, Masenelli-Varlot K, Dendievel R, Cavaille JY, et al. Multi-walled carbon nanotube/polymer nanocomposites: processing and properties. *J Polym Sci B: Polym Phys* 2005;43(10):1186–97.
- [7] Wang DW, Lu JG, Otten CJ, Buhro WE. Electrical transport in boron nanowires. *Appl Phys Lett* 2003;83(25):5280–2.
- [8] Wang DW, Wang Q, Javey A, Tu R, Dai HJ, Kim H, et al. Germanium nanowire field-effect transistors with SiO<sub>2</sub> and high-kappa HfO<sub>2</sub> gate dielectrics. *Appl Phys Lett* 2003;83(12):2432–4.
- [9] Wang DW, Otten CJ, Buhro WE, Lu JG. Rectifying effect in boron nanowire devices. *IEEE Trans Nanotechnol* 2004;3(2):328–30.
- [10] Cao H, Wang Q, Wang DW, Dai HJ. Suspended carbon nanotube quantum wires with two gates. *Small* 2005;1(1):138–41.
- [11] Javey A, Tu R, Farmer DB, Guo J, Gordon RG, Dai HJ. High performance *n*-type carbon nanotube field-effect transistors with chemically doped contacts. *Nano Lett* 2005;5(2):345–8.
- [12] Chen LH, Jin S. Packaging of nanostructured microelectromechanical systems microtriode devices. *J Electron Mater* 2003;32(12):1360–5.
- [13] Fukuda T, Arai F, Dong LX. Assembly of nanodevices with carbon nanotubes through nanorobotic manipulations. *Proc IEEE* 2003;91(11):1803–18.
- [14] Husain A, Hone J, Postma HWC, Huang XM, Drake T, Barbic M, et al. Nanowire-based very-high-frequency electromechanical resonator. *Appl Phys Lett* 2003;83(6):1240–2.
- [15] Matkovich VI. Boron and refractory borides. Berlin: Springer-Verlag; 1977.
- [16] Tavazdeh FN, Lominadze JV, Khvedelidze AG, Tsagareishvili GV, Shorshorov MK, Bulichev SI. The effect of impurities on the mechanical-properties of zone-melted boron. *J Less-Common Metals* 1981;82(1–2):95–9.
- [17] Cooper HS. Boron. In: Hampel CA, editor. Rare metals handbook. London: Reinhold Publishing Corporation; 1954. p. 69–81.
- [18] Otten CJ, Lourie OR, Yu MF, Cowley JM, Dyer MJ, Ruoff RS, et al. Crystalline boron nanowires. *J Am Chem Soc* 2002;124(17):4564–5.
- [19] Poncharal P, Wang ZL, Ugarte D, de Heer WA. Electrostatic deflections and electromechanical resonances of carbon nanotubes. *Science* 1999;283(5407):1513–6.
- [20] Wang ZL, Poncharal P, de Heer WA. Nanomeasurements of individual carbon nanotubes by in situ TEM. *Pure Appl Chem* 2000;72(1–2):209–19.
- [21] Dikin DA, Chen X, Ding W, Wagner G, Ruoff RS. Resonance vibration of amorphous SiO<sub>2</sub> nanowires driven by mechanical or electrical field excitation. *J Appl Phys* 2003;93(1):226–30.
- [22] Bai XD, Gao PX, Wang ZL, Wang EG. Dual-mode mechanical resonance of individual ZnO nanobelts. *Appl Phys Lett* 2003;82(26):4806–8.
- [23] Meirovich L. Elements of vibration analysis. New York: McGraw-Hill; 1975. p. 212.
- [24] Yu MF, Lourie O, Dyer MJ, Moloni K, Kelly TF, Ruoff RS. Strength and breaking mechanism of multi-walled carbon nanotubes under tensile load. *Science* 2000;287(5453):637–40.
- [25] Tan EPS, Lim CT. Novel approach to tensile testing of micro- and nanoscale fibers. *Rev Sci Instrum* 2004;75(8):2581–5.
- [26] Tan EPS, Ng SY, Lim CT. Tensile testing of a single ultrafine polymeric fiber. *Biomaterials* 2005;26(13):1453–6.
- [27] Zussman E, Chen X, Ding W, Calabri L, Dikin DA, Quintana JP, et al. Mechanical and structural characterization of electrospun PAN-derived carbon nanofibers. *Carbon* 2005;43:2175–85.

- [28] Yu MF, Dyer MJ, Skidmore GD, Rohrs HW, Lu XK, Ausman KD, et al. Three-dimensional manipulation of carbon nanotubes under a scanning electron microscope. *Nanotechnology* 1999;10(3):244–52.
- [29] Ding W, Dikin DA, Chen X, Piner R, Ruoff RS, Zussman E, et al. Mechanics of hydrogenated amorphous carbon deposits from electron beam induced deposition of a paraffin precursor. *J Appl Phys* 2005;98:014905.
- [30] Chen X, Zhang SL, Wagner GJ, Ding W, Ruoff RS. Mechanical resonance of quartz microfibers and boundary condition effects. *J Appl Phys* 2004;95(9):4823–8.
- [31] Yu MF, Wagner GJ, Ruoff RS, Dyer MJ. Realization of parametric resonances in a nanowire mechanical system with nanomanipulation inside a scanning electron microscope. *Phys Rev B* 2002;66(7):073406.
- [32] Huang Z, Dikin DA, Ding W, Qiao Y, Chen X, Fridman Y, et al. Three-dimensional representation of curved nanowires. *J Microsc-Oxford* 2004;216:206–14.
- [33] Xu TT, Zheng JG, Wu NQ, Nicholls AW, Roth JR, Dikin DA, et al. Crystalline boron nanoribbons: synthesis and characterization. *Nano Lett* 2004;4(5):963–8.
- [34] Brodhag C, Thevenot F. Hot-pressing of various boron phases. *J Less-Common Metals* 1986;117(1–2):175–80.
- [35] JCPDS-International Centre for Diffraction Data, PCPDFWIN, v. 2.4; 2003.
- [36] Lide DR, editor. *CRC handbook of Chemistry and Physics*. 78th ed. Boca Raton, FL: CRC Press; 1997.
- [37] Bridge B, Patel ND, Waters DN. On the elastic-constants and structure of the pure inorganic oxide glasses. *Phys Status Solidi a- Appl Res* 1983;77(2):655–68.
- [38] Chen X, Zhang SL, Dikin DA, Ding W, Ruoff RS, Pan LJ, et al. Mechanics of a carbon nanocoil. *Nano Lett* 2003;3(9):1299–304.
- [39] Ding W, Eitan A, Fisher FT, Chen X, Dikin DA, Andrews R, et al. Direct observation of polymer sheathing in carbon nanotube-polycarbonate composites. *Nano Lett* 2003;3(11):1593–7.
- [40] Sader JE, Larson I, Mulvaney P, White LR. Method for the calibration of atomic-force microscope cantilevers. *Rev Sci Instrum* 1995;66(7):3789–98.
- [41] Zhu Y, Moldovan N, Espinosa HD. A microelectromechanical load sensor for in situ electron and X-ray microscopy tensile testing of nanostructures. *Appl Phys Lett* 2005;86(1):013506.
- [42] Yu MF, Files BS, Arepalli S, Ruoff RS. Tensile loading of ropes of single wall carbon nanotubes and their mechanical properties. *Phys Rev Lett* 2000;84(24):5552–5.
- [43] Li XD, Wang XN, Chang WC, Chao YJ, Chang M. Effect of tensile offset angles on micro/nanoscale tensile testing. *Rev Sci Instrum* 2005;76(3):033904–5.
- [44] Talley CP. Mechanical properties of glassy boron. *J Appl Phys* 1959;30(7):1114–5.
- [45] Talley CP. Preparation of single-crystal boron. *J Appl Phys* 1961;32(9):1787–8.
- [46] Layden GK. Fracture behavior of boron filaments. *J Mater Sci* 1973;8(11):1581–9.
- [47] Boggio JV, Vingsbo O. Tensile-strength and crack nucleation in boron fibers. *J Mater Sci* 1976;11(2):273–82.
- [48] Carlsson JO, Lundstrom T. Mechanical-properties and surface defects of boron fibers prepared in a closed CVD system. *J Mater Sci* 1979;14(4):966–74.
- [49] Carlsson JO. Morphologies of boron fibers in the temperature-range 1000 to 1500 °C and the relationship between mechanical-properties and morphology. *J Mater Sci* 1979;14(11):2726–32.
- [50] Carlsson JO. Techniques for the preparation of boron fibers. *J Mater Sci* 1979;14(2):255–64.
- [51] Ochiai S, Abe K, Osamura K. Preparation of boron fiber reinforced aluminum matrix composites and their deformation and fracture-behavior. *J Jpn Inst Metals* 1984;48(10):1028–34.
- [52] Luo ZP, Sun CY. Effect of the interfacial bonding status on the tensile fracture characteristics of a boron-fiber-reinforced aluminum composite. *Mater Character* 2003;50(1):51–8.